PHYSICAL REVIEW B **79**, 165426 (2009)

Thermodynamics of adsorption of light alkanes and alkenes in single-walled carbon nanotube bundles

Fernando J. A. L. Cruz and José P. B. Mota[*]

Departamento de Química, Requimte/CQFB, Faculdade de Ciências e Tecnologia, Universidade Nova de Lisboa,
2829-516 Caparica, Portugal

(Received 21 January 2009; published 20 April 2009)

The thermodynamics of adsorption of light alkanes and alkenes (CH_4, C_2H_6, C_2H_4, C_3H_8, and C_3H_6) in single-walled carbon nanotube bundles is studied by configurational-bias grand canonical Monte Carlo simulation. The bundles consist of uniform nanotubes with diameters in the range 11.0 Å$\leq D \leq$18.1 Å, arranged in the usual close-packed hexagonal lattice. The phase space is systematically analyzed with calculations for adsorption at room temperature and reduced pressure range of $8.7\times 10^{-9} < p/p_0 < 0.9$. The simulation results are interpreted in terms of the molecular nature of the adsorbate and the corresponding solid-fluid interactions. It is shown that confinement in the internal volume of the bundle (interstitial and intratubular) is energetically more favorable than physisorption on the external surface (grooves and exposed surfaces of peripheral tubes), as indicated by the curves of isosteric heat as a function of reduced pressure. However, the zero-loading properties suggest a crossover point to this behavior for $D \sim 18-19$ Å. When interstitial confinement is not inhibited by geometrical considerations, it is possible to establish the following ordering of the zero-loading isosteric heat by type of adsorption site: $(q_{st}^0)^{\text{interstitial}} > (q_{st}^0)^{\text{intratubular}} > (q_{st}^0)^{\text{grooves}} > (q_{st}^0)^{\text{surface}}$.

DOI: 10.1103/PhysRevB.79.165426 PACS number(s): 82.60.Qr, 61.46.Fg, 64.75.Jk

I. INTRODUCTION

Molecular confinement in nanoscale pores is of fundamental and applied importance for a wide range of physical, chemical, and biological processes.[1–7] As model nanopores of cylindrical geometry, single-walled carbon nanotubes (SWCNTs) (Refs. 8 and 9) have been receiving considerable attention due to their unique and exciting features, such as optical[10] and electronic properties.[11] Among several applications,[12] SWCNTs have been proposed as building blocks for composites,[13] chemical sensors,[14] separating agents of organic vapors,[15] and as storage nanomaterials for hydrogen[16] and methane.[17,18] In many cases the application of SWCNTs involves the interaction of organic fluids with their solid lattice by means of physisorption confinement. Similarly to a graphene sheet, SWCNTs exhibit a π-electron cloud around their walls, arising from the sp^2 hybridization of the carbons atoms. Due to strong van der Waals interactions[1] resulting from this charge distribution, SWCNT samples are usually obtained as a collection of individual tubes aggregated in the form of heterogeneous spaghettilike structures called bundles.[19]

As depicted in Fig. 1, for the usual hexagonal lattice[20–22] the available adsorption sites are distributed over the internal porous volume of the bundle (intratubular void space and interstices) but also over its external surface (grooves and exposed surfaces of the peripheral tubes). The existence of distinct types of adsorption sites is a fundamental difference between SWCNTs and other carbon materials, such as activated carbon, that needs to be addressed in any accurate study of the adsorptive properties of these structured nanomaterials. For example, both the interstices and grooves can be interpreted as quasilinear arrays for the physical realization of matter in one dimension.[23,24] However, interstitial adsorption is only possible if the individual nanotube diameter is large enough.[25] Moreover, both the internal volume of a nanotube and the exposed surface of the outermost nanotubes of a bundle can physisorb a molecule in a variety of different adsorbate configurations, resulting in two- or even three-dimensional adsorption. Because these sites are intrinsically different, their force fields exhibit differences in the energetic landscape that can be ultimately related to measurable properties such as individual tube diameter, bulk fluid pressure (or chemical potential), and temperature. We shall address this interesting issue in the present study.

Due to its spherical geometry and well characterized physical properties, methane is one of the most commonly used probe molecules to study the thermodynamics of adsorption in SWCNT bundles.[18,20,23–31] Properties such as the isosteric heat of adsorption, q_{st}, have been used as effective parameters to monitor the mechanism of physisorption confinement. Kowalczyk *et al.*[18] have performed grand canonical Monte Carlo (GCMC) simulations of CH_4 adsorbed onto an homogenous (10,10) SWCNT bundle at 293 K, considering only interstitial and intratubular adsorption. They concluded that q_{st} increases nonlinearly with adsorbate loading up to a total maximum of 20.5 kJ/mol, and decreases henceforward. A similar bundle was employed by Jiang *et al.*[32] to study the adsorption of linear alkanes C_n $(n \leq 5)$ at 300 K; these authors reported zero-loading isosteric heats in the range 18.3–53.4 kJ/mol.

Recently, LaBrosse *et al.*[25] addressed the adsorption of CH_4 on heterogeneous and homogeneous bundles, using simulation techniques and low-temperature (77 K) measurements. The isotherms and isosteric heats for the groove sites and outside surface of heterogeneous bundles were found to be very close to those for the homogeneous bundles, indicating that bundle heterogeneity is of little consequence to external adsorption. This is not surprising if one takes into account that, for a small molecule such as methane, the external surface of the bundle can behave similarly to a planar graphene sheet, depending on the spacing between adjacent

©2009 The American Physical Society

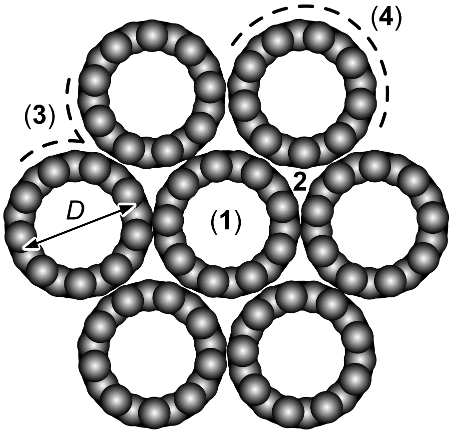

FIG. 1. Different adsorption sites in an homogeneous bundle of SWCNTs with individual tube diameter D: (1) intratubular, (2) interstitial channel, (3) external groove, (4) external rounded surface. Sites 1 and 2 comprise the internal pore volume of the bundle, whereas sites 3 and 4 are both located on the external surface of the bundle.

tubes. A similar premise was postulated by Shi *et al.*[28] who observed that groove sites located in either homogeneous or heterogeneous closed-ended bundles are indeed very similar. An interesting experimental study was conducted by Bienfait *et al.*[29] on homogeneous bundles of closed-ended SWCNTs with 17 ± 1 Å tube diameters. Although the intratubular volume was neglected, their study clearly showed two preferential adsorptive sites on the sample, as evidenced by two plateaus in the curve of q_{st} against coverage. The grooves and interstitial sites exhibited roughly 62% higher values of q_{st} than the exposed surface of the peripheral tubes. The adsorption simulations and neutron diffraction experiments with closed-ended homogeneous SWCNT bundles of Johnson *et al.*[24] seem to corroborate the idea that interstitial and groove sites are energetically more favorable for adsorption than surface sites, and therefore are the ones being initially populated by adsorbed CH_4 molecules.

The aforementioned studies are prominent examples of starting contributions to the effort of building up a molecular-level picture of the phenomena governing adsorption onto structured, multisite nanoporous materials. However, an unabridged understanding of the microscopic details involved is still incomplete, particularly in the case of intratubular adsorption, whose mechanism is known to play a predominant role in the low-pressure limit.[33] Among other issues that also need careful investigation is the choice of the probe molecule itself, which can be either spherical or linear, as well as its spatial orientation.[34] Two of the simplest examples of linear probe molecules are ethane (C_2H_6) and ethylene (C_2H_4), whose main difference between them is the existence of an unsaturated π bond in ethylene; this type of unsaturated chemical bond introduces a certain degree of rigidity into the molecule and at the same time makes it smaller compared with the saturated analog. How do the structure and chemical nature of the probe molecule influence the thermodynamic properties of adsorption? What is the relationship between q_{st} and molecular length, expressed in terms of the number of carbon atoms of the molecular skeleton? Because of geometric impediment it is expected that some interstitial channels will not be physically available to all adsorbate molecules; this sieving effect is essentially governed by two parameters: (i) the individual tube diameter of the three confining SWCNTs, and (ii) the molecular diameter of the adsorptive fluid.

We have already presented a detailed structural analysis of commercially available SWCNT bundles,[19,35] which was validated by comparison with Raman scattering and experimental adsorption data of several organic fluids,[36,37] nitrogen,[19] and water.[38] In the present work, we address the particular case of an ideal sample comprising homogeneous, open-ended SWCNT bundles. Experimentally, samples are usually prepared as heterogeneous bundles, with some nanotube ends blocked, possessing a distribution of individual tube diameters[35] in the range $11.0\ \text{Å} \leq D \leq 18.1\ \text{Å}$. However, it is possible to sort out the individual tubes according to their diameter as well as to treat the sample with physicochemical processes to unblock the closed ends.[39–42]

In the present work we report a systematic GCMC (Refs. 43–45) simulation study of adsorption, at room temperature, of CH_4, C_2H_6, C_2H_4, C_3H_8, and C_3H_6, onto the different sites of ideal SWCNT homogeneous bundles (both inter- and intratubular volume, grooves, and external rounded surface). The pressures explored in the simulations ($10^{-7}\ \text{bar} < p < 105\ \text{bar}$) span a relative pressure range of $8.7\times10^{-9} < p/p_0 < 0.9$, where p_0 is the saturation pressure of the vapor adsorptive. By eliminating impurities, polydispersity in nanotube diameter, and pore blockage, we are addressing the most favorable bundle structure for application of SWCNTs as membranes, molecular sieves, and gas storage media.

The remaining of the paper is organized as follows. In Sec. II, the force field and simulation methodology are described along with the model employed for the bundle geometry. In Sec. III, the calculated isosteric heats of adsorption and molecular density curves are discussed and interpreted in terms of the chemical nature of the probe molecules and of the structural characteristics of the bundle. The extrapolation of data toward the limit of very low pressure allows the determination of the isosteric heat of adsorption at zero loading, and the corresponding study of the solid-fluid interactions. Comparisons are drawn with experimental data whenever these are available. Finally, the work is summarized and conclusions drawn.

II. MOLECULAR MODELS AND SIMULATION DETAILS

The force field adopted for the five adsorbates, methane $[CH_4(sp^3)]$, ethane $[CH_3(sp^3)-CH_3(sp^3)]$, ethylene $[CH_2(sp^2)=CH_2(sp^2)]$, propane $[CH_3(sp^3)-CH_2(sp^3)-CH_3(sp^3)]$, and propylene $[CH_2(sp^2)=CH(sp^2)-CH_3(sp^3)]$, is the transferable potential for phase equilibria (TraPPE).[46,47] This force field is based on an united-atom (UA) model where the $CH_4(sp^3)$, $CH_3(sp^3)$, $CH_2(sp^3)$, $CH_2(sp^2)$, and $CH(sp^2)$ groups are treated as single interaction sites. The nonbonded interactions between pseudoatoms on different adsorbate molecules, as well as the interactions between carbon atoms of a nanotube[48–50] and pseudoatoms of adsorbate molecules, are governed by the Lennard-Jones (LJ) 12–6 potential,

TABLE I. Lennard-Jones parameters for the TraPPE-UA force field (Refs. 46 and 47) and for the SWCNT atoms (Refs. 48–50).

Pseudoatom	ϵ_i/k_B (K)	σ_i (Å)
C (SWCNT)	28.0	3.400
CH_4 (methane)	148.0	3.730
CH_3 (sp^3)	98.0	3.750
CH_2 (sp^3)	46.0	3.950
CH_2 (sp^2)	85.0	3.675
CH (sp^2)	47.0	3.730

$$u(r_{ij}) = 4\epsilon_{ij}[(\sigma_{ij}/r_{ij})^{12} - (\sigma_{ij}/r_{ij})^{12}], \tag{1}$$

where r_{ij} is the intermolecular distance between sites i and j. The potential well depths, ϵ_i/k_B (k_B is the Boltzmann constant), and collision diameters, σ_i, are listed in Table I. The cross terms are obtained using the classical Lorenz-Berthelot combining rules,[44,51] $\epsilon_{ij}=(\epsilon_i\epsilon_j)^{1/2}$ and $\sigma_{ij}=(\sigma_i+\sigma_j)/2$. A spherical potential truncation for pairs of pseudoatoms separated by more than 14 Å is enforced,[46] and analytical tail corrections are not applied.

In the TraPPE-UA force field all bond lengths are fixed; the length of the CH_x-CH_y bond is 1.54 Å, whereas that of the CH_x=CH_y is 1.33 Å. The harmonic bond-bending potential, $u_{\text{bend}}(\theta)$, along the three pseudoatoms of either propane or propylene is given by $u_{\text{bend}}(\theta)=k_\theta(\theta-\theta_0)^2/2$. For propane, the force constant is $k_\theta/k_B=62500$ K/rad^2 and the equilibrium bending angle is $\theta_0=114.0°$; the corresponding values for propylene are $k_\theta/k_B=70420$ K/rad^2 and $\theta_0=119.7°$.

At ambient temperature the SWCNTs can be reasonably approximated as smooth structureless nanocylinders. For a pseudoatom of an adsorbate molecule located at a nearest distance δ from the central axis of a nanotube, an effective potential, $U_{\text{sf}}(\delta)$, is developed by integrating the LJ solid-fluid potential, $u_{\text{sf}}(r)$, over the positions of all wall atoms of the nanotube (whose length is assumed to be infinite),

$$U_{\text{sf}}(\delta) = 4\rho_s R \int_0^\pi u_{\text{sf}}(r)\, d\theta\, dz, \quad r^2 = R^2 + \delta^2 - 2\delta R \cos\theta. \tag{2}$$

Here, $R=D/2$ is the pore radius, z is the distance along the cylinder axis, θ is the radial angle, and $\rho_s=0.382$ Å^2 is the atomic surface density of the SWCNT wall. By integrating over z and θ, Eq. (2) is reduced to a one-dimensional (1D) potential that is a function of δ only,

$$U_{\text{sf}}(\delta) = \pi^2\rho_s\epsilon_{\text{sf}}\sigma_{\text{sf}}^2\left[\frac{63\Phi(9,\delta/R)}{32\gamma^{10}} - \frac{3\Phi(3,\delta/R)}{\gamma^4}\right], \tag{3a}$$

$$\gamma = \frac{R-\delta}{\sigma_{\text{sf}}}\left(1+\frac{\delta}{R}\right), \tag{3b}$$

$$\Phi(\alpha,\beta) = F\left(-\frac{\alpha}{2},-\frac{\alpha}{2},1;\beta^2\right), \tag{3c}$$

where $F(\alpha,\beta,\gamma;\delta)$ is the hypergeometric function. To speedup the calculation of $U_{\text{sf}}(\delta)$, Eq. (3a) is tabulated on a grid with 31 kn equally spaced in δ^2. During the simulations $U_{\text{sf}}(\delta)$ is reconstructed from the tabulated information using cubic Hermite polynomial interpolation.

Figure 2 shows the cross sections of the unit cells for building the simulation boxes to study adsorption in the internal pore volume of the bundle and onto its external surface. The unit cells depicted in Figs. 2(a) and 2(b) are for intrabundle adsorption, whereas that shown in Fig. 2(c) is for adsorption on the external surface of the bundle. It is worth noting that only the gray areas represent effective volume probed during the simulation; thus, the unit cell of Fig. 2(a) comprises the internal volume of a cylinder, that in Fig. 2(b) is a parallelepiped, and the one in Fig. 2(c) is obtained by subtracting one-quarter of a cylinder from the two bottom edges of a parallelepiped. The nanotubes in Fig. 2(b) are arranged in the usual close-packed hexagonal lattice. The intertubular distance for all simulations is kept fixed at 3.4 Å to mimic SWCNTs adhering to each other via van der Waals forces forming bundles.

The actual length of each simulation box is a function of the imposed adsorptive pressure, to sample at least 20 molecules on average, but always larger than twice the spherical potential truncation of 14 Å. The size of the simulation box for intratubular adsorption is adjusted by changing the length of the cylinder in Fig. 2(a) along the z coordinate. To adjust the size of the simulation box for combined intratubular and interstitial adsorption, the unit cell of Fig. 2(b) is replicated along the x and y coordinates, as many times as necessary. The size of the simulation box for external adsorption is adjusted by replicating the unit cell of Fig. 2(c) along the x coordinate. The faces of each simulation box implement periodic boundary conditions, except for the top face of the box in Fig. 2(c), which is a reflecting wall, and the bottom face of the same box, which is blocked by the outermost shell of nanotubes in the bundle.

To calculate the solid-fluid interaction potential of a pseudoatom located inside a nanotube of the bundle, it suffices to sum the interactions of the pseudoatom with the confining tube and with the its six nearest neighbors. The corrugation effect of the neighboring tubes is very small and, for practical purposes, does not affect the cylindrical symmetry of the total interaction potential. Therefore, when only intratubular adsorption is of interest it is computationally more efficient to employ the cylindrical simulation box shown in Fig. 2(a), which consists of the intratubular volume of a single nanotube under a force field that includes the additional contribution from the six nearest-neighboring tubes.

The simulation box shown in Fig. 2(b) is employed to study the combined effect of intratubular adsorption and adsorption in the interstitial channels (where three tubes meet). An interstitial region can be divided into three symmetric volumes with pentagonal-like cross sections (some of the edges are denoted by the dotted lines). The solid-fluid potential for a pseudoatom in one of those volumes is calculated

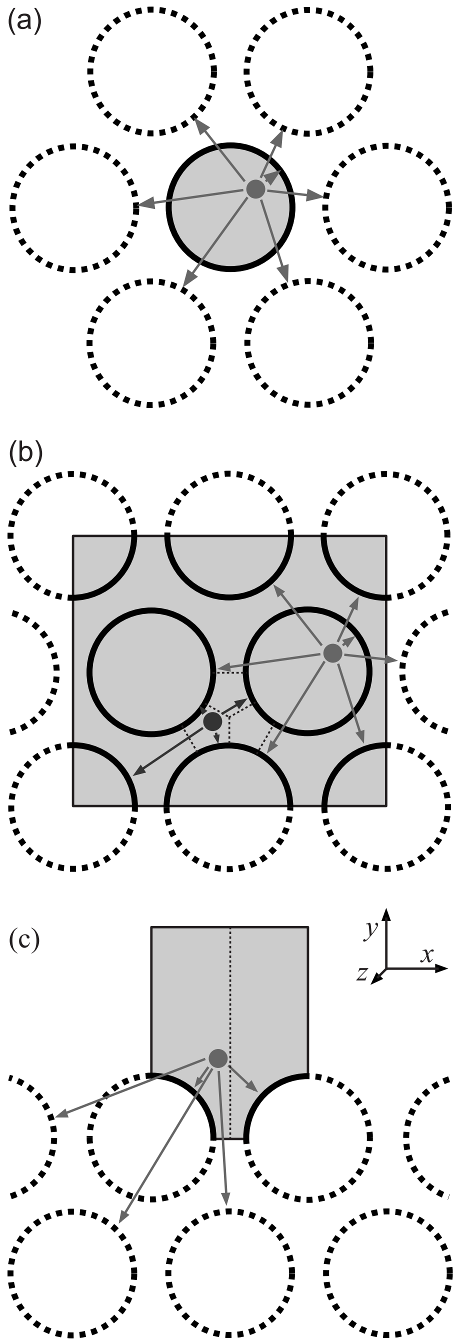

FIG. 2. Cross sections of the unit simulation cells for GCMC simulation of fluid adsorption onto different adsorption sites of an homogeneous bundle of open-ended SWCNTs: (a) intratubular volume; (b) intratubular and interstitial channels; (c) external surface (grooves and exposed surface of the peripheral tubes). The gray area represents the effective volume probed during the simulations.

by summing the interactions of the pseudoatom and the four nearest tubes, as indicated in Fig. 2(b) by the dark arrows. We have observed that including farther nanotubes does not significantly change the interaction potential.[52]

Figure 2(c) shows the cross section of the unit simulation box for GCMC study of adsorption onto the exterior volume of a bundle. It has been shown previously[52] that to determine the overall interaction potential between a pseudoatom of a sorbate molecule and the peripheral surface of the bundle it suffices to consider the interactions between the pseudoatom and its five nearest nanotubes (three on the outermost shell and two on the second shell). Including farther nanotubes has a minimum impact on the total solid-fluid interaction potential. Notice that the nanotubes are not part of the simulation box itself and, therefore, molecules are not allowed to adsorb inside of them.

To enhance the sampling of configurational space and increase the acceptance rate of the molecule insertion or removal step for the largest adsorbates (propane and propylene), we resort to configurational-bias sampling techniques.[53–56] In the configurational-bias method a flexible molecule is grown atom-by-atom toward energetically favorable conformations, leading to a scheme which is orders of magnitude more efficient than the traditional method of random growth.

For the placement of the first pseudoatom of an adsorbate molecule, $k_1=10$ random positions in the simulation box are generated, and one is selected with a probability $\exp(-\beta U_{1,i}^{\text{ext}})/\Sigma_j \exp(-\beta U_{1,j}^{\text{ext}})$, where $\beta=1/k_{\text{B}}T$ and $U_{1,j}^{\text{ext}}$ is the external energy of the pseudoatom at the jth trial position interacting with the nanotubes and with the pseudoatoms of the other adsorbate molecules. For each of the remaining two pseudoatoms ($m=2,3$) of the molecule, $k_m=5$ trial positions are generated with a probability proportional to $U_{m,i}^{\text{ext}}$. These positions are distributed on the surface of a sphere centered on the previously inserted pseudoatom of the molecule and whose radius is equal to the bond length. Each set of k_m trial orientations is generated using the internal part of the potential $U_{m,j}^{\text{int}}$, whose probability depends on which type of pseudoatom is being inserted; for the second atom ($m=2$) the internal potential energy is zero and, as a result, the trial positions are randomly distributed on a sphere; for the third pseudoatom ($m=3$) the internal potential energy includes bond bending. For $m=3$ the trial positions are distributed on the edge of the disk which forms the base of a cone with apex at the center of the previously inserted bead and slant height equal to the bond length. For each trial position j ($j=1,\ldots,k_m$) the external energy $U_{m,j}^{\text{ext}}$ is calculated for interaction with the nanotubes, with the pseudoatoms of the other adsorbate molecules. From among the k_m trial positions, one is selected with a probability $\exp(-\beta U_{m,i}^{\text{ext}})/\Sigma_j \exp(-\beta U_{m,j}^{\text{ext}})$. During this growth process a bias is introduced, but is removed by adjusting the acceptance rules.

Besides the usual trial step of molecule insertion-deletion, where the acceptance rate is enhanced by resorting to configurational-bias techniques, three additional types of Monte Carlo (MC) move involving only individual molecules are necessary to sample the internal configuration of the simulation box: translation, rotation about the center of mass, and configurational-bias partial regrowth to change the internal conformation of a molecule.

Each run is equilibrated for at least 2×10^4 Monte Carlo cycles followed by at least an equal number of cycles for the production period. Each cycle consists of $0.8N$ attempts to translate a randomly selected molecule, $0.2N$ trial rotations, $0.2N$ attempts to change the conformation of a molecule using configurational-bias partial regrowth, and $\max(20,0.2N)$ molecule insertion-deletion steps. Here, N is the number of molecules in the simulation box at the beginning of each cycle. The maximum displacement for translation and angle for rotation are adjusted during the equilibration phase to give a 50% acceptance rate. Standard deviations of the ensemble averages are computed by breaking the production run into five blocks. The imposed fugacity of the coexisting bulk fluid is converted into pressure by the Peng-Robinson equation of state with parameters taken from Ref. 57.

III. RESULTS AND DISCUSSION

The GCMC simulations are carried out for room temperature (298.15 K) and reduced pressures in the range $8.7\times10^{-7} < p/p_0 < 0.9$, where p_0 is the saturation pressure of the fluid[58] at the simulation temperature. For C_3H_8 and C_3H_6 the lower limit of p/p_0 is decreased to 8.7×10^{-9}. The isosteric heat of adsorption, q_{st}, is directly related to the amount of heat released when a molecule adsorbs on a solid substrate. This quantity can be calculated from statistical-mechanical considerations[43] as

$$q_{\mathrm{st}} = \frac{\langle U\rangle\langle N\rangle - \langle UN\rangle}{\langle N^2\rangle - \langle N\rangle\langle N\rangle} + k_{\mathrm{B}}T, \tag{4}$$

where $\langle\ \rangle$ denotes the ensemble average, N is the number of molecules in the simulation box, U is the configurational energy of the system, k_{B} is the Boltzmann constant, and T is the imposed temperature.

During the course of a simulation of intratubular or interstitial adsorption, every fluid molecule present in one of the simulation boxes shown in Figs. 2(a) and 2(b) is clearly in an adsorbed state and is an effective probe molecule for the configurational space of the adsorbed phase. On the other hand, the fluid molecules located in the upper region of the simulation box for studying external adsorption [Fig. 2(c)] are part of the coexisting bulk fluid and not of the adsorbed phase. This problem is always present when studying adsorption onto open surfaces. In order to avoid any ambiguity, it is best to work with an excess quantity which is determined by subtracting the contribution from the coexisting bulk phase. To do this, we compute the bulk isosteric heat, $q_{\mathrm{st}}^{\mathrm{G}}$, and ensemble average number of molecules, $\langle N_{\mathrm{g}}\rangle$, when the solid-fluid interaction potential is zero, $U_{\mathrm{sf}}=0$. The excess isosteric heat, $(q_{\mathrm{st}})^{\mathrm{ex}}$, for adsorption on the external surface of the bundle is then determined as

$$(q_{\mathrm{st}})^{\mathrm{ex}} = \frac{\langle q_{\mathrm{st}}\rangle\langle N\rangle - q_{\mathrm{st}}^{\mathrm{G}}\langle N_{\mathrm{g}}\rangle}{\langle N\rangle - \langle N_{\mathrm{g}}\rangle}. \tag{5}$$

The values of q_{st} obtained from the simulations are plotted in Fig. 3 as a function of p/p_0 and D for the various adsorbates. The dispersion in the external adsorption data for methane is statistical and does not influence the general trends of the q_{st} curves. Note that the upper and lower sets of curves represent the distinct contributions from internal (intratubular and interstitial) and external (grooves and exposed surfaces of the peripheral tubes) adsorption, respectively.

To determine the distribution of molecules between the four different adsorption sites (cf. Fig. 1), we calculate the fractional contribution of the groove sites to external adsorption, as well as the fractional contribution of the intratubular volume to internal adsorption. For this purpose, we define a fractional loading for groove sites as $N^{(\mathrm{g,s})}/N^{(\mathrm{s})}$, where $N^{(\mathrm{g,s})}$ is the number of molecules in the grooves and $N^{(\mathrm{s})}$ is the total number of adsorbed molecules in the external sites (grooves and exposed surfaces of the peripheral tubes). Similarly, the fractional loading for intratubular adsorption is defined as $N^{(\mathrm{i,v})}/N^{(\mathrm{v})}$, where $N^{(\mathrm{i,v})}$ is the number of molecules inside the nanotubes, and $N^{(\mathrm{v})}$ is the total number of adsorbed molecules in the internal volume of the bundle (tubes and interstices).

Before proceeding with a detailed analysis of the results, some general trends can already be established. The value of q_{st} for internal adsorption is always larger than for external adsorption, and this difference becomes particularly relevant in the medium-to high-pressure region; for $p/p_0 > 10^{-2}$ the difference increases from 5–10 to 10–25 kJ/mol as $p/p_0 \rightarrow 1$ and the molecular weight increases. It is clear from Fig. 3 that the value of q_{st} for external adsorption is quite independent of D; by contrast, the value of q_{st} for the adsorptive contribution of the internal volume of the bundle varies markedly with diameter. The latter trend is less clear as the fluid approaches saturation and the diameter becomes a less relevant factor. At high-pressure entropy is the dominant thermodynamical variable, as opposed to energy under vacuum or very low pressure.

A. Internal adsorption: Intratubular space and interstitial channels

As shown in Fig. 3, after an initial flat plateau q_{st} increases nonlinearly with pressure up to a maximum value, $q_{\mathrm{st}}^{\max}$. Our value of $q_{\mathrm{st}}^{\max}$ for CH_4 in 13.8 Å nanotubes, 21.5 ± 0.3 kJ/mol, is in very good agreement with the previously reported value of 20.5 kJ/mol for an homogeneous (10,10) bundle ($D=13.56$ Å).[18] This maximum results from the optimum interplay between the solid-fluid and fluid-fluid interaction energies. At higher adsorbate loadings (relative pressure) the fluid-fluid interactions become more and more intense, caused by the condensation of fluid due to the imposed chemical potential, and therefore the isosteric heat exhibits a decreasing trend with pressure.

The calculated values of $q_{\mathrm{st}}^{\max}$ are listed in Table II for all diameters studied in this work. The results show two general trends: (i) $q_{\mathrm{st}}^{\max}$ increases with the decrease in D, reflecting the enhanced solid-fluid interaction in smaller nanotubes, and (ii) $q_{\mathrm{st}}^{\max}$ increases with the number of carbon atoms on the probe adsorptive, essentially due to the increase in the number of interaction sites per adsorbate molecule. Moreover, it is evident from Table II that the saturated molecules exhibit larger isosteric heats than their corresponding unsaturated analogs, although those differences are relatively minor (1–3.9 kJ/mol).

We can postulate a threshold of $N^{(\mathrm{i,v})}/N^{(\mathrm{v})}=0.995$, above which it can be considered that, within the statistical error of the calculations, all adsorbed molecules are confined inside the tubes and thus interstitial adsorption can be safely neglected. By inspection of Fig. 4 it is concluded that interstitial adsorption is always inhibited for the smaller nanotube

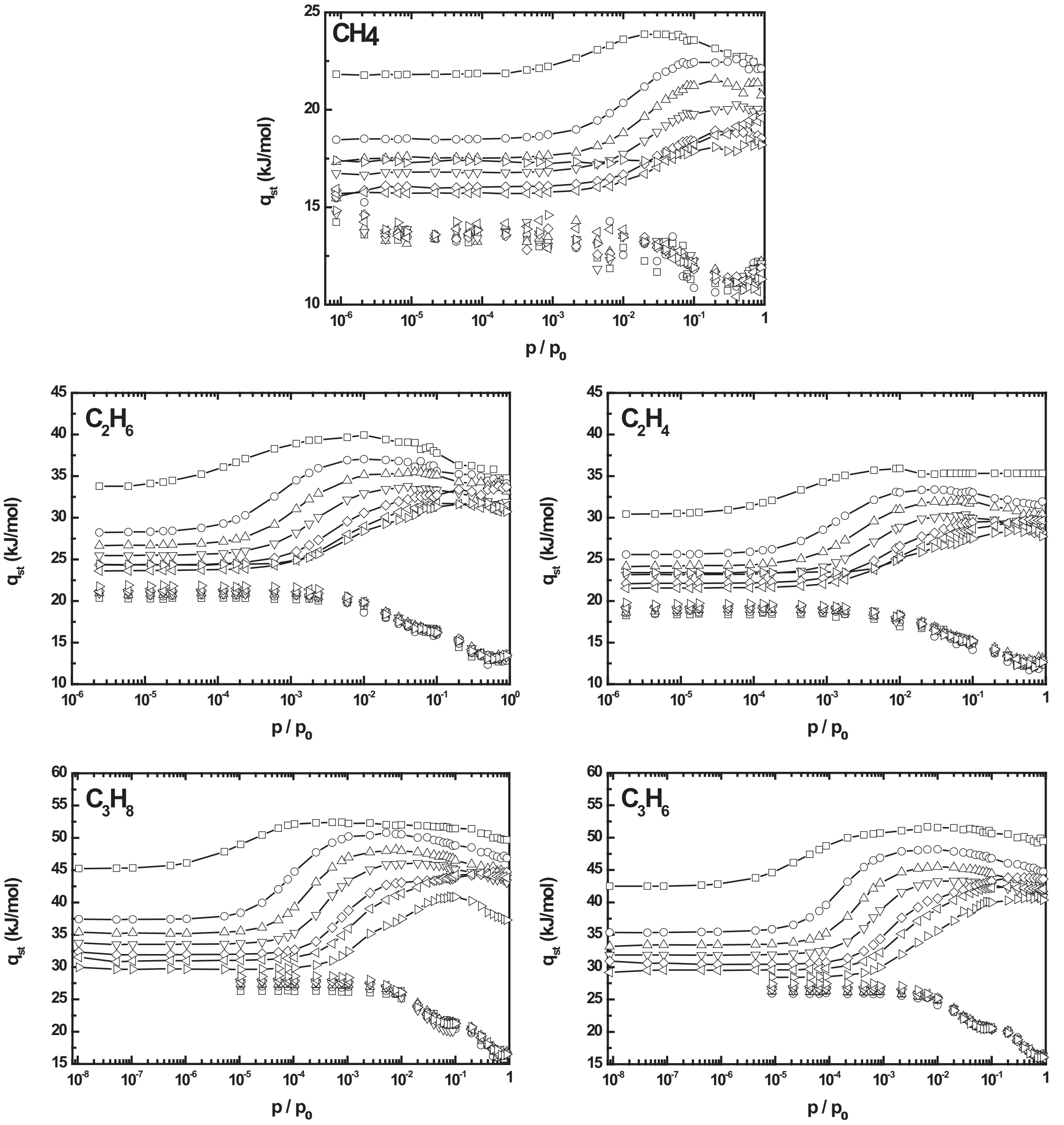

FIG. 3. Isosteric heat of adsorption, q_{st}, as a function of reduced pressure, p/p_0, and tube diameter, D, for the internal volume of the bundle (upper curves), comprising intratubular and interstitial sites, and for the external surface (lower curves), comprising grooves and exposed surfaces of the peripheral tubes. Note that for C_3H_8 and C_3H_6, p/p_0 is extended down to 8.7×10^{-9} to validate the general trends for internal adsorption. Solid lines are guides to the eyes. □ 11.0 Å, ○ 12.9 Å, △ 13.8 Å, ▽ 14.7 Å, ◇ 15.8 Å, ◁ 16.6 Å, ▷ 18.1 Å.

diameters, 11.0 Å $\leq D \leq$ 14.7 Å. This has to do with geometrical impediments of the interstitial channels themselves, which are too narrow to physically accommodate fluid molecules. A different situation is observed for larger diameter tubes (15.8 and 16.6 Å), which form interstices wide enough to adsorb particles, at least under medium- to high-pressure conditions. The largest diameter studied, 18.1 Å, exhibits an extreme case, where significant interstitial adsorption can occur even in the low-pressure limit ($p/p_0 < 10^{-3}$). It now becomes clear that the initial plateau in Fig. 3 corresponds mainly to intratubular adsorption; the plateau remains horizontal while molecules are being adsorbed into the annular layer around the inner nanotube wall.

A very interesting case happens for 11.0 Å, whose plateau is markedly further away from the main group of curves. For this narrow diameter, not only molecules are not interstitially adsorbed, but they also fit tightly into the nanotubes, lying with an orientation parallel to the central tube axis. As previously mentioned, the exception is the case for D=18.1 Å, where molecules are initially adsorbed both in the interstitial and intratubular sites, and whose corresponding q_{st} curves are above the lines for D=16.6 Å. This phenomenon is observed for CH_4, C_2H_6, and C_2H_4, but not for C_3H_8 or C_3H_6 because of their larger molecular sizes.

To illustrate these adsorption mechanisms, we have produced contour plots of the adsorbate concentration field inside equilibrated simulation boxes, and represented them on the xy plane perpendicular to the central axis z of the nanotubes. For conciseness, we only show contour plots for methane, at two different diameters and reduced pressures; these

TABLE II. Maximum value of the isosteric heat of adsorption, $q_{\mathrm{st}}^{\mathrm{max}}$, for the internal pore volume of the bundle, for each individual tube diameter studied. Subscripts give the uncertainty in the last digit.

D (Å)	$q_{\mathrm{st}}^{\mathrm{max}}$ (kJ/mol)				
	CH_4	C_2H_6	C_2H_4	C_3H_8	C_3H_6
11.0	23.9_1	39.8_2	35.9_1	52.4_4	51.7_6
12.9	22.6_3	37.0_4	33.4_3	50.8_1	48.2_1
13.8	21.5_3	35.5_4	32.1_5	48.2_4	45.5_1
14.7	20.3_4	33.8_2	30.4_3	46.1_1	43.3_3
15.8	19.3_4	33.8_6	29.6_3	44.7_1	43.8_3
16.6	19.6_4	31.7_2	29.8_6	44.5_4	42.4_2
18.1	18.5_4	31.8_5	28.6_3	42.0_4	41.0_7

plots are, nevertheless, representative of the main cases occurring in the whole phase and fluid space (Fig. 5). Starting with the lowest diameter [Fig. 5(a)], it is evident that interstitial adsorption is totally absent and that intratubular confinement is the only relevant adsorption mechanism. If we now move to the highest tube diameter, equilibrated at a low reduced pressure [Fig. 5(b)], it is observed that the molecules are confined both in the interstices and in the intratubular volume. As pressure increases, the intratubular monolayer approaches completion and q_{st} approaches its maximum value. Upon reaching the maximum, q_{st} starts to decrease due to the formation of an intratubular condensed phase oriented parallel to the central tube axis [Fig. 5(c)].

The contour plot of intratubular molecular density displayed in Fig. 5(c) represents a typical case where two phases coexist inside the nanotube: one corresponding to a monolayer of molecules adsorbed close to the cylindrical wall, and the other to a second condensed phase in the central intratubular core. This type of radial density distribution has been observed in the largest tubes for all fluids studied.

We can define a radial density profile for the molecular center of mass, $\rho(r)$, where r is the radial distance to the nanotube central axis. The plots of $\rho(r)$ are reproduced in Fig. 6 for the smallest (11.0 Å) and largest (18.1 Å) nanotube diameters. The results for C_2H_4 and C_3H_6 in 11.0 Å nanotubes are very similar to their saturated analogs; for clarity sake they are not explicitly shown in the graph. The intensity of each peak is proportional to the number density of molecules that can be accommodated in a differential annular volume whose cross-sectional area is proportional to rdr; as expected it decreases from smaller to larger molecules. Also, because unsaturated molecules are slightly smaller, the peak intensity also increases slightly with respect to that of the corresponding saturated analog by less than 5%.

It is worth noting that very different fluid structures are observed in the two limiting cases of molecular confinement. While for $D=11.0$ Å the molecules form only one annular adsorbed layer, arranged around the wall [Figs. 5(a) and 6], for $D=18.1$ Å the intratubular volume is large enough to accommodate a second concentric layer of fluid, whose structure is dependent on the carbon skeleton of the molecule. For the temperature explored here, methane and ethylene are supercritical fluids, so one cannot objectively discuss the existence of a liquid phase. However, all fluids exhibit an annular layer of adsorbed molecules adjacent to the inner wall, with density that decreases with the number of carbon atoms, as evidenced by the two highest peaks shown in Fig. 6 for both $D=11.0$ Å and $D=18.1$ Å. In this layer, the molecular center of mass has mobility along the axial coordinate z and angular coordinate θ, but is strongly constrained in the radial coordinate r. In the inner core, fluids can also form a second intratubular phase, located around the nanotube center ($r=0$), whose structure is dependent on the molecular identity. For methane and ethylene, which are the smallest adsorbates, the shape of the inner layer is a smeared annular cylinder; for the other adsorbates, however, the inner layer comprises a single row of molecules with decreasing lateral mobility as their molecular size increases.

The densities plotted in Fig. 6 are based on a nanotube volume defined by the skeletal diameter D of the tube (Fig. 1), as measured by the distance between centers of opposite carbon atoms on the wall. From the point of view of molecular simulation this definition is very convenient, but it is inconsistent with the accurate thermodynamic setting of the solid-fluid boundary as already pointed out elsewhere.[59,60] Inspection of Fig. 6 clearly shows the existence of a nonnegligible annular space adjacent to the wall that is not accessible to fluid molecules; this exclusion volume arises from the strong short-ranged repulsive interactions between fluid and nanotube. A physically realistic definition for the thickness δ of that repulsive annular layer is the largest distance from the solid wall over which the radial profile of molecular center of mass density is zero; using this definition we obtain $\delta \approx 2.80$ (CH_4), 2.95 (C_2H_6), 2.95 (C_2H_4), 3.30 (C_3H_8), and 3.35 Å (C_3H_6). Previous calculations at lower temperatures (210–240 K) have determined $\delta \approx 3.15$ Å for C_3H_8,[61] in very good agreement with our present result.

B. External adsorption: Grooves and exposed surface of peripheral tubes

Similarly to what is observed for molecular confinement in the internal volume of the bundle, the curve of q_{st} against p/p_0 for external adsorption also starts as an horizontal plateau (Fig. 3), persistent until $p/p_0 \approx 10^{-3}$. It then decreases

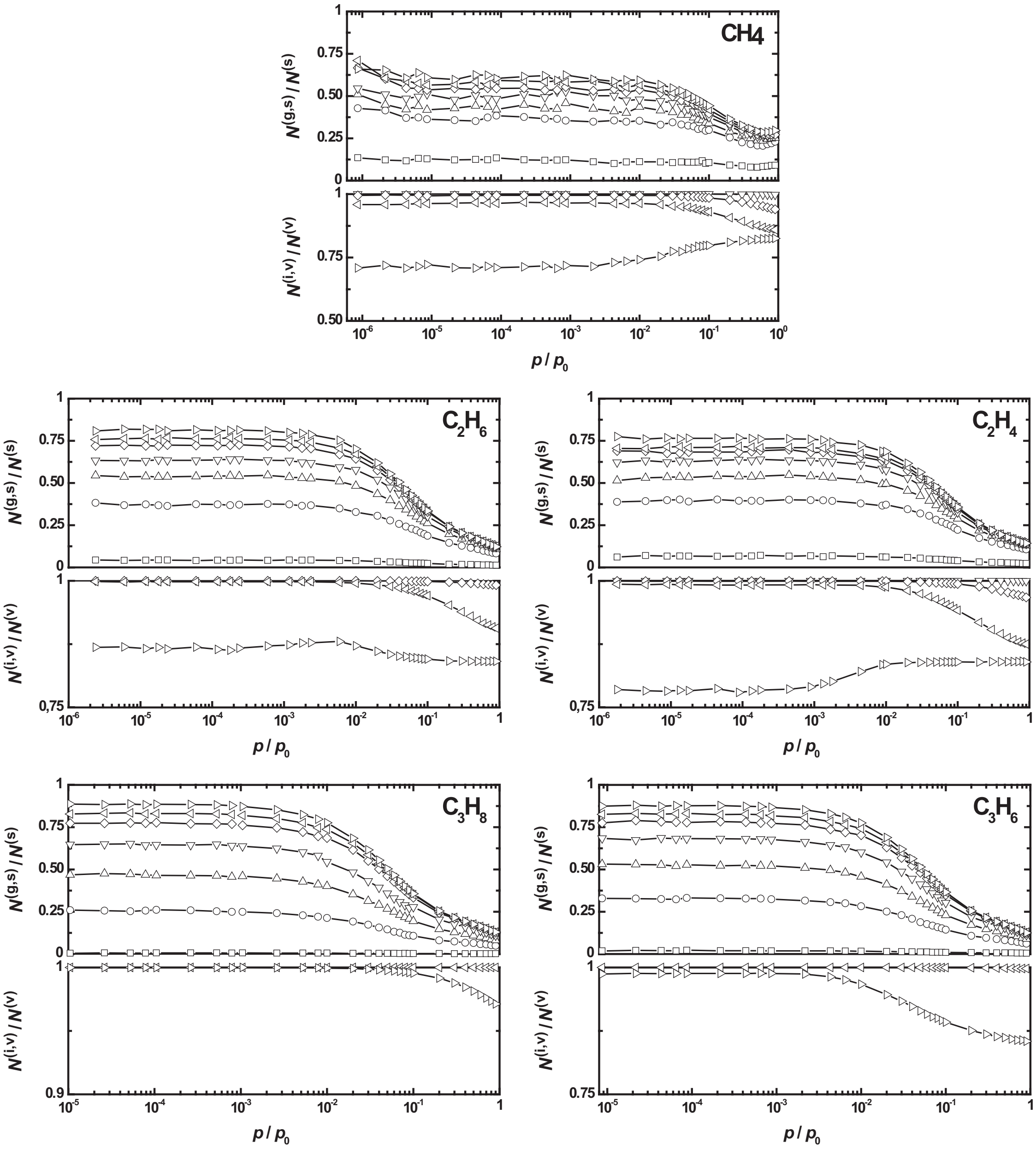

FIG. 4. Number ratios of adsorbed molecules, $N^{(i,v)}/N^{(v)}$ and $N^{(g,s)}/N^{(s)}$, for endohedral and external adsorption, respectively; $N^{(i,v)}$ is the number of molecules adsorbed in the intratubular space, $N^{(v)}$ is the number of molecules adsorbed in the overall internal volume of the bundle (tubes and interstices), $N^{(g,s)}$ is the number of molecules adsorbed into the groove sites, and $N^{(s)}$ is the number of molecules adsorbed on all external sites (grooves and exposed surfaces of the peripheral tubes). Solid lines are guides to the eyes. □ 11.0 Å, ○ 12.9 Å, △ 13.8 Å, ▽ 14.7 Å, ◇ 15.8 Å, ◁ 16.6 Å, ▷ 18.1 Å.

toward a second (smaller) plateau, after which it keeps decreasing until there is complete condensation of the fluid. The general decreasing behavior of q_{st} with coverage is in agreement with what has been previously observed in experimental adsorption measurements of ethane onto bundles of closed-ended SWCNTs.[62] Representative contour plots of the adsorbate concentration field for the second plateau of the q_{st} curve and for near condensation conditions are shown in Fig. 7 for propane adsorption onto the external surface of bundles with 14.7 Å nanotubes. The contour plots of molecular density for the first plateau are similar to that of Fig. 7(a) but without visual traces of adsorbate over the exposed surfaces of the peripheral tubes.

Closed-end nanotubes with small diameters do not exhibit interstitial adsorption, so they essentially possess external surface and groove sites available to physisorb molecules. Our q_{st} curves highlight the existence of two different types of external adsorption sites available for fluid molecules, as evidenced by the two distinct plateaus mentioned above. Calbi *et al.*[23] performed detailed energy calculations for the external surface of an homogeneous bundle, and concluded that groove sites are energetically more favorable for methane adsorption than surface sites. A similar conclusion was reached by Johnson *et al.*,[24] who have shown that groove sites exhibit larger binding energies[63] than surface sites. The first plateau in our q_{st} curves is therefore attributed to mo-

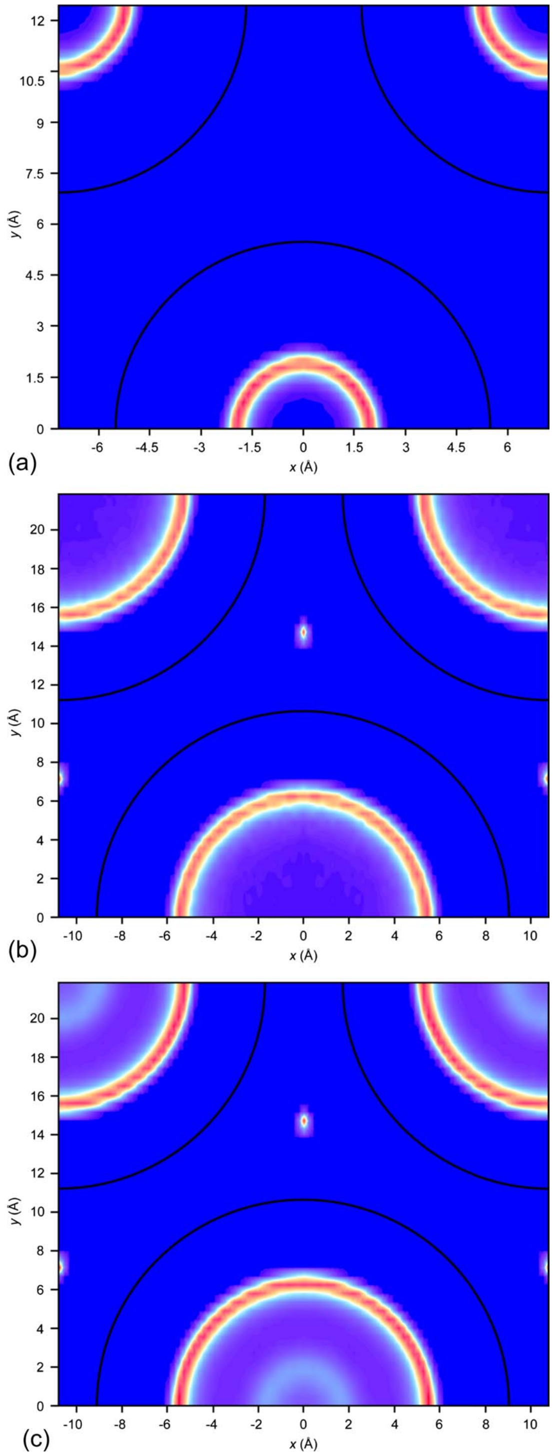

FIG. 5. (Color online) Contour plots of molecular density, $\rho(x,y)$, for adsorbed CH_4, on the $x\times y$ plane perpendicular to the central axis of the nanotubes. Data plotted for (a) $D=11.0$ Å and $p/p_0=0.9$, (b) $D=18.1$ Å and $p/p_0=0.01$, (c) $D=18.1$ Å and $p/p_0=0.9$. The molecular density increases from dark blue to red. The solid black lines locate the centers of the carbon atoms on the nanotube walls. In the central graph (b) the color scale for interstitial adsorption is 17 times larger than for intratubular adsorption; in the bottom graph (c) it is 12 times larger. Note the absence of interstitial adsorption for $D=11.0$ Å (a), and the low-density central core for $D=18.1$ Å under low-pressure conditions (b).

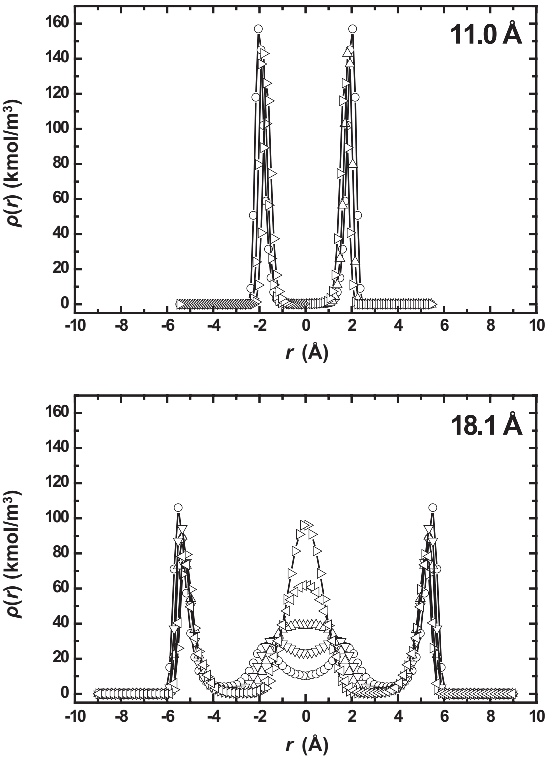

FIG. 6. Radial profiles of adsorbate density, $\rho(r)$, in the intratubular volume of a bundle for $p/p_0=0.9$ and two different tube diameters (11.0 Å and 18.1 Å); $r=0$ denotes the central tube axis. For simplicity, the results for C_2H_4 and C_3H_6 in 11.0 Å nanotubes are not plotted, they are analogous to those for C_2H_6 and C_3H_8 (see the text for details). ○ CH_4, △ C_2H_6, ▽ C_2H_4, ▷ C_3H_8, ◁ C_3H_6.

lecular adsorption into the groove sites, whereas the second one is due to monolayer completion on the exposed surface of the peripheral nanotubes.

In Fig. 4 we plot the ratio of the number of molecules in groove sites, $N^{(g,s)}$, to the number $N^{(s)}$ of molecules in all external adsorption sites (grooves and curved surfaces); by definition, when $N^{(g,s)}/N^{(s)}>0.5$ there will be more externally adsorbed molecules in the groove sites than on the peripheral surfaces. A closer inspection of Fig. 4 shows that in the low-pressure region the predominance of groove adsorption increases with nanotube diameter, and that there is a threshold at $D\approx 13.8$ Å above which the groove sites are more populated with molecules than the exposed surface of the peripheral tubes. For propane in bundles of 18.1 Å nanotubes, $N^{(g,s)}/N^{(s)}\approx 0.89$. Once the grooves become filled, adsorption proceeds onto the exposed surface of the peripheral tubes as pressure increases and thus $N^{(g,s)}/N^{(s)}$ starts decreasing. Cruz *et al.*[33] have observed that propane and propylene adsorption onto an homogenous bundle of 18.1 Å diameter nanotubes, occurs initially in groove sites between two adjacent tubes. Above the threshold of 13.8 Å while groove occupation is weakly dependent on D, adsorption of molecules onto surface sites is rather independent of that geometric constraint. This is not surprising if one bears in mind that the dimensions of a groove site are more diameter dependent than those of the adjacent curved surfaces. In fact, previous calculations of methane adsorption onto surface sites have

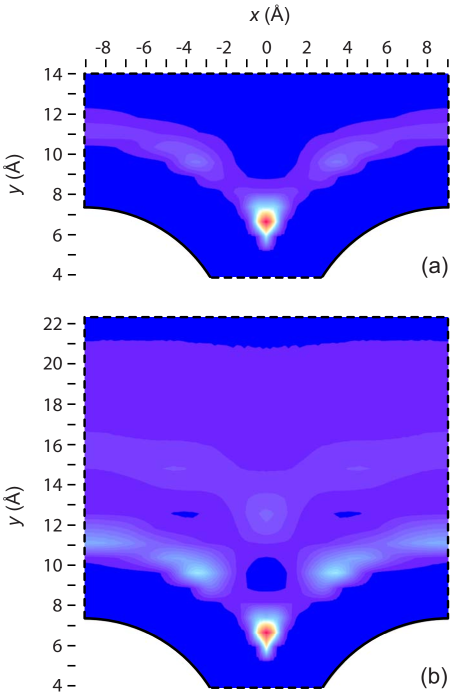

FIG. 7. (Color online) Contour plots of molecular density on the $x \times y$ plane, $\rho(x,y)$, for propane adsorbed onto the external sites of bundles with 14.7 Å nanotubes. Data plotted for (a) p/p_0=0.08 (second horizontal plateau of the q_{st} curve in Fig. 4) and (b) p/p_0 =0.9 (near condensation conditions). The molecular density increases from dark blue to red. The solid black arcs locate the centers of the carbon atoms on the nanotube walls.

shown that for a small molecule as methane, the binding energy for external adsorption is independent of D.[24] In the present study this finding is corroborated for methane but also verified for the other chain molecules.

The second plateau of the q_{st} curves for external adsorption is more pronounced for propane and propylene than for the other adsorbates, because of their longer molecular chain and their ability to bend their carbon skeleton, thus enhancing the solid-fluid interaction along the rounded outer surface of a nanotube. From the second plateau of the q_{st} curves plotted in Fig. 3 we have determined average values of the isosteric heat, $q_{\mathrm{st}}^{\mathrm{s}}$, for adsorption onto the exposed surface of the peripheral tubes. The calculated values are plotted in Fig. 8, which shows that $q_{\mathrm{st}}^{\mathrm{s}}$ is independent of the tube diameter. The values of $q_{\mathrm{st}}^{\mathrm{s}}$ averaged over all tube diameters are 12.48 ± 0.05 (CH_4), 16.45 ± 0.05 (C_2H_6), 15.13 ± 0.05 (C_2H_4), 21.27 ± 0.14 (C_3H_8), and 20.59 ± 0.02 kJ/mol (C_3H_6).

For the subcritical fluids (ethane, propane and propylene) at the temperature studied here, the value of $q_{\mathrm{st}}^{\mathrm{s}}$ can be extrapolated to the limit $p/p_0=1$ in order to estimate their enthalpy of vaporization, ΔH_{vap}. The extrapolation for all tube diameters of a least-squares fitting of the $q_{\mathrm{st}}^{\mathrm{s}}$ data for $p/p_0 > 0.5$ produced the following estimates of ΔH_{vap}: 13.4 ± 0.1 (C_2H_6), 16.3 ± 0.1 (C_3H_8), and 16.0 ± 0.1 kJ/mol (C_3H_6).

The small standard deviations for the estimated values of ΔH_{vap} show that they are rather independent of the tube diameter, as it should be for any bulk property. The obtained values of ΔH_{vap}, 9.76 (C_2H_6), 16.25 (C_3H_8), and 16.04 kJ/mol (C_3H_6), are consistent with experimental data.[64]

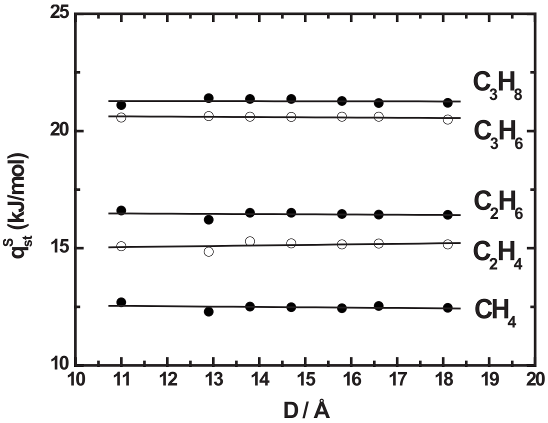

FIG. 8. Isosteric heat of adsorption, $q_{\mathrm{st}}^{\mathrm{s}}$, as a function of tube diameter, D, for the exposed surface of the peripheral tubes of a bundle. The statistical error is smaller than the size of the symbols.

C. Isosteric heat of adsorption at zero-loading

Under high-vacuum conditions, near the zero-loading region, the fluid-fluid contribution to the isosteric heat of adsorption can be safely neglected, thus allowing one to get further insight into the nature of the solid-fluid interactions. To estimate the isosteric heat at zero loading, q_{st}^{0}, the data plotted in Fig. 3 were extrapolated to the limit $p \to 0$. The individual values of q_{st}^{0} for the internal volume and for the external surface of the bundle are plotted in Fig. 9.

As discussed above, the lighter fluids (methane, ethane and ethylene) can be adsorbed into the interstitial channels, even at low pressure, if D is larger than given threshold values, ca. 15.8 (CH_4), 16.6 (C_2H_4), and 18.1 Å (C_2H_6). This is particularly relevant for the larger diameters studied here, where interstitial adsorption at low pressure can ac-

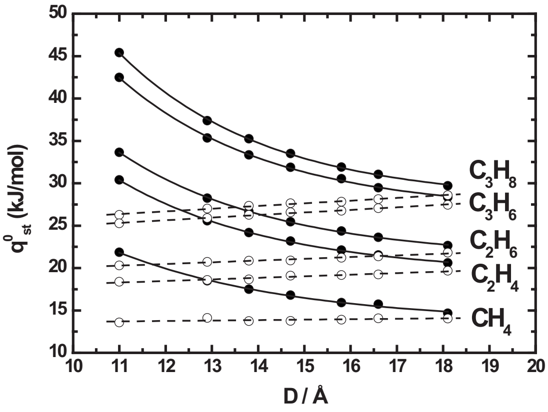

FIG. 9. Isosteric heat of adsorption at zero loading, q_{st}^{0}, for the internal volume (filled symbols) and external surface (open symbols) of a bundle as a function of tube diameter D. Calculated values of q_{st}^{0} for CH_4, C_2H_6, and C_2H_4 in 18.1 Å nanotubes do not include the contribution from interstitial confinement (see text for details). Symbols are calculated data and lines are either linear (dashed) or first-order exponential (solid) fittings [Eq. (7)].

count for 14–29 % of the total internal adsorption, but rather unimportant for the smaller diameters where its contribution never exceeds 1–5 %. Keeping this in mind, it is worth noting that we have excluded the contribution of interstitial adsorption from the values of q_{st}^{0} plotted in Fig. 9 for $D = 18.1$ Å, in order to keep them in line with the q_{st}^{0} values for the other tube diameters. We have calculated the values of q_{st}^{0} for $D = 18.1$ Å, taking interstitial adsorption into account; they deviate ca. 18% (CH_4), 8% (C_2H_4), and 13% (C_2H_4) from their purely intratubular counterparts.

From Fig. 9 a general trend can be established, namely, that q_{st}^{0} scales with the molecular weight. As molecular weight increases from C_1 to C_3, so does the number of interaction sites on the molecule (pseudoatoms), thus enhancing the fluid interactions with the solid wall. The open symbols in Fig. 9 show that for external adsorption q_{st}^{0} increases linearly with D,

$$(q_{\mathrm{st}}^{0})^{(\mathrm{s})} = \alpha + \beta D, \tag{6}$$

with increasing, but gentle slope β. When internal adsorption is considered, q_{st}^{0} is seen to decrease with D according to a first-order exponential decay (closed symbols in Fig. 9),

$$(q_{\mathrm{st}}^{0})^{(\mathrm{v})} = \alpha + \beta \exp(-D/\gamma). \tag{7}$$

The data plotted in Fig. 9 suggest that there is a value of D above which q_{st}^{0} is larger for external adsorption than that for adsorption in the internal volume of the bundle, when the former replaces the latter as the region of the bundle with the most energetically favorable adsorption sites. The crossover seems to be somewhere within the range $D = 18-19$ Å. This observation is particularly interesting and has been previously overlooked. For $D > 19$ Å, two things are expected to occur: (i) the tube diameter is so large that the peripheral surface of the bundle looses its corrugation effect, and behaves instead as a periodic sequence of rounded surfaces and low valleys (grooves); (ii) the intratubular cross section becomes so large that molecules no longer feel the attraction of the curved wall at the opposite side of the tube where they adsorb, thus behaving as if they were attracted by a single graphite sheet.

We have performed a least-squares fitting of the dependency of q_{st}^{0} on D for the internal volume of the bundle and for its external surface; the regressed values are listed in Table III. For comparison purposes, we have also calculated the value of q_{st}^{0} for adsorption on a single graphene layer and for adsorption on an infinite number of stacked layers. The interaction potential between a Lennard-Jones site of an adsorbate molecule and a single graphene sheet is given by Steele's 10–4 potential,[48]

$$U_{\mathrm{sf}}(z) = 2\pi\rho_{\mathrm{s}}\epsilon_{\mathrm{sf}}\sigma_{\mathrm{sf}}^{2}\left[\frac{2}{5}\left(\frac{\sigma_{\mathrm{sf}}}{z}\right)^{-10} - \left(\frac{\sigma_{\mathrm{sf}}}{z}\right)^{-4}\right], \tag{8}$$

where z is the shortest distance between the adsorbate site and the graphene layer, $\rho_{\mathrm{s}} = 0.382$ Å^{2} is the atomic surface density of graphite, and ϵ_{sf} and σ_{sf} are the solid-fluid cross-term parameters. If the adsorbate interacts with an infinite number of stacked graphene sheets, with interlayer spacing $\Delta_{\mathrm{s}} = 3.4$ Å, then the interaction energy can be calculated according to a 10–4-3 potential,[48]

$$U_{\mathrm{sf}}(z) = 2\pi\rho_{\mathrm{s}}\epsilon_{\mathrm{sf}}\sigma_{\mathrm{sf}}^{2} \times \left[\frac{2}{5}\left(\frac{\sigma_{\mathrm{sf}}}{z}\right)^{-10} - \left(\frac{\sigma_{\mathrm{sf}}}{z}\right)^{-4} - \frac{\sigma_{\mathrm{sf}}^{4}}{3\Delta_{\mathrm{s}}(0.61\Delta_{\mathrm{s}}+z)^{3}}\right]. \tag{9}$$

TABLE III. Isosteric heat of adsorption at zero loading, q_{st}^{0} (kJ/mol), for different adsorption sites of a SWCNT bundle and limiting values of D: internal volume [v, $D \to \infty$, α in Eq. (7)], intratubular space (i, $D = 18.1$ Å), interstitial channels (ic, $D = 18.1$ Å), and external sites [s, $D \to 0$, α in Eq. (6)]. For comparison purposes, experimental (G^X) and calculated values (single layer, G^1; infinite number of stacked layers, G^∞) of q_{st}^{0} for graphite are also included. Subscripts give the uncertainty in the last digit.

q_{st}^{0}	CH_4	C_2H_6	C_2H_4	C_3H_8	C_3H_6
v	13.5_4	21.1_0	19.3_2	27.9_3	26.6_3
i[a]	14.7_0	22.6_0	20.6_0		
ic[a]	24.1_0	35.2_1	33.1_3		
s	13.1_4	18.1_2	16.3_3	22.9_2	22.0_2
G^X	14.9[b]	16.0		24.8	
		19.7[c]		27.3[c]	
G^1	9.13_7	14.64_9	13.23_5	19.20_9	18.39_7
G^∞	10.85_9	17.37_9	15.70_7	22.74_8	21.68_6

[a] Data for $D = 18.1$ Å in the range $8 \times 10^{-7} < p/p_0 < 9 \times 10^{-3}$.
[b] Determined at 77 K (Ref. 29).
[c] Determined at 300 K (Ref. 65).

The asymptotic value of q_{st}^{0} for intratubular adsorption in the limit of a very large tube diameter can be estimated from the value of α in Eq. (7). For methane, $\alpha = 13.5$ kJ/mol is close to the experimental value of 14.9 kJ/mol for methane adsorption onto the basal plane of graphite,[29] confirming our previous arguments that there is a finite and limiting diameter above which intratubularly confined molecules behave as if they were adsorbed onto a planar surface. A similar observation holds for external adsorption when the tube diameter is so narrow that the grooves loose their corrugation effect and the external surface of the bundle behaves as a stack of planar graphene sheets. For this limiting case we obtained the value of 13.1 kJ/mol for methane, which is also in reasonable agreement with the experimental value for adsorption onto the basal plane of graphite and with our own calculated value of 10.85 kJ/mol for adsorption onto an infinite number of stacked graphene layers.

Comparison of our results for internal and external adsorption of C_2H_6 and C_3H_8 indicates that for both cases our calculated data are in satisfactory agreement with experimental measurements.[65] Jiang *et al.*[32] have calculated the values of q_{st}^{0} for methane, ethane, and propane adsorption on homogeneous, open-ended bundles with $D = 13.56$ Å. Since interstitial adsorption is inhibited for this tube diameter, the reported q_{st}^{0} values, 18.27 (CH_4), 27.71 (C_2H_6), and 35.86 kJ/mol (C_3H_8), can be considered as resulting from intratubular confinement only. These data compare remarkably well with

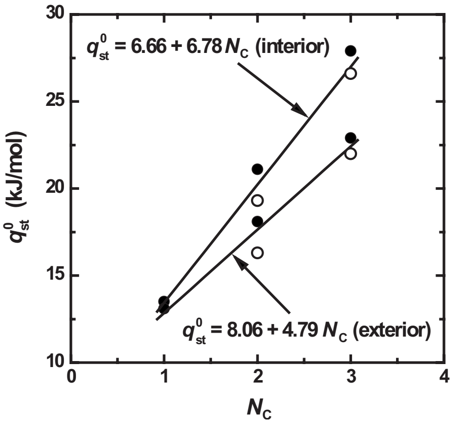

FIG. 10. Isosteric heats at zero loading, q^0_{st}, for internal (v) and external adsorption (s), as function of the number of carbon atoms on the probe molecule, N_C. CH_4, C_2H_6, and C_3H_8 (filled symbols), C_2H_4 and C_3H_6 (open symbols).

our values calculated for $D=13.8$ Å: 17.49 (CH_4), 26.66 (C_2H_6), and 35.25 kJ/mol (C_3H_8).

For $D=18.1$ Å we have separated the individual contributions to q^0_{st} of intratubular and interstitial adsorption. The value of q^0_{st} for interstitial adsorption is larger than the value for intratubular confinement by ca. 60%, and this difference is quite independent from molecular length or chemical nature (Table III). For such large tube diameters, molecules in the interstitial channels experience adsorption in a nanovolume with enhanced solid-fluid interaction resulting from the confinement between three different nanotube walls. On the other hand, the molecules inside a large tube behave as if they were confined in a slit-pore geometry, of large spacing, and thus subject to weaker solid-fluid interactions. Therefore, due to energetic considerations, the latter is expected to be less favorable for adsorption than the former.

It is known that at low pressure, adsorption onto the external surface of the bundle starts in the groove sites, and proceeds to the surface sites as the chemical potential is increased.[23,29] Therefore, the values of $\lim_{D\to\infty} q^0_{st}$ listed in Table III for external adsorption are a good measure of the zero-loading isosteric heats for the groove sites. As expected, interstitial sites exhibit larger isosteric heats than the groove sites located in the bundle with largest tube diameter (cf. Table III). Indeed, energy calculations of methane adsorption onto closed-ended heterogeneous bundles, point out to the fact that for large D the interstitial sites have equal or higher isosteric heats than the groove sites.[23,28]

The values of q^0_{st} listed in Table III are plotted in Fig. 10 as a function of the number of carbon atoms, N_c, of the adsorbate molecule. The linear trends obtained for both internal and external adsorption are not unexpected. For internal adsorption (intratubular and interstitial), the linear dependence of q^0_{st} with the number of carbon atoms has been observed before for a bundle with $D=13.56$ Å.[32] The present results not only corroborate these findings, but also extend the same conclusions to external adsorption and to unsaturated molecules. From the inspection of Fig. 10, it can be observed that q^0_{st} for CH_4 is rather insensitive to either internal or external adsorption, but this similarity does not hold for longer molecules since the two values of q^0_{st} start to diverge from each other, as the number of carbon atoms increases. The curve of q^0_{st} against N_c for internal adsorption indicates a stronger dependence of the isosteric heat on the number of carbon atoms of the adsorbate molecule, as evidenced by the larger slope of the linear trend.

IV. CONCLUSIONS

Using an idealized geometrical model of a SWCNT bundle, as an approximation to those found in real samples, we have studied the local adsorption potential for the four different adsorptive sites of the bundle, and established general trends in the isosteric heat against relative pressure and tube diameter. From the plots of the intratubular radial concentration profiles, it was possible to estimate a physically realistic distance, δ, of closest approach of a fluid molecule to the nanotube wall; this distance decreases with the number of carbon atoms on the fluid molecule. The results obtained for the isosteric heat at zero loading provide valuable information on the nature of the solid-fluid interactions.

External adsorption was found to be rather independent of the individual tube diameter (cf. Fig. 7), and in the low-pressure region adsorption into the grooves prevails over the other external surface sites. On the other hand, the calculated q^0_{st} values for intrabundle confinement are very dependent on D, but its dependency tends to smear out and reach an asymptotic behavior as D increases. Confinement in the internal volume of the bundle is always energetically more favorable than external adsorption, over the whole pressure range, and that difference increases with pressure and molecular weight. Interstitial adsorption is only significant for the largest diameter studied (18.1 Å), but for that diameter it is energetically more favorable than intratubular confinement. However, a previously unaccounted threshold seems to exist at $D \sim 18-19$ Å, above which external adsorption dominates over intrabundle confinement. In the present study, low-pressure interstitial adsorption is only relevant for methane and the C_2 adsorbates for $D=18.1$ Å. For these cases, it is possible to establish the following ordering for the zero-loading isosteric heat of adsorption: $(q^0_{st})^{\text{interstitial}} > (q^0_{st})^{\text{intratubular}} > (q^0_{st})^{\text{grooves}} > (q^0_{st})^{\text{surface}}$.

ACKNOWLEDGMENTS

Financial support from the Luso-American Foundation for Development (FLAD, Portugal), and FCT/MCTES (PT) through Grant No. SFRH/BPD/45064/2008, is gratefully acknowledged.

*pmota@dq.fct.unl.pt

[1] A. N. Khlobystov, D. A. Britz, and G. A. D. Briggs, Acc. Chem. Res. **38**, 901 (2005).

[2] C. Alba-Simionesco, B. Coasne, G. Dosseh, K. E. Gubbins, R. Radhakrishnan, and M. Sliwinska-Bartkowiac, J. Phys.: Condens. Matter **18**, R15 (2006).

[3] B. Trzaskowski, A. F. Jalbout, and L. Adamowicz, Chem. Phys. Lett. **430**, 97 (2006).

[4] W. Yang, P. Thordarson, J. J. Gooding, S. P. Ringer, and F. Braet, Nanotechnology **18**, 412001 (2007).

[5] P. Kondratyuk and J. John T. Yates, J. Am. Chem. Soc. **129**, 8736 (2007).

[6] A. Alexiadis and S. Kassinos, Chem. Eng. Sci. **63**, 2047 (2008).

[7] P. Szabelski, J. Chem. Phys. **128**, 184702 (2008).

[8] R. Saito, G. Dresselhaus, and M. S. Dresselhaus, *Physical Properties of Carbon Nanotubes* (Imperial College Press, London, 1998).

[9] M. Meyyappan, *Carbon Nanotubes: Science and Applications* (CRC Press, London, 2005).

[10] J. A. Fagan, J. R. Simpson, B. J. Bauer, S. H. De Paoli Lacerda, M. L. Becker, J. Chun, K. B. Migler, A. R. H. Walker, and E. K. Hobbie, J. Am. Chem. Soc. **129**, 10607 (2007).

[11] A. Taherpour, Fullerenes, Nanotubes, Carbon Nanostruct. **15**, 279 (2007).

[12] R. H. Baughman, A. A. Zakhidov, and W. A. de Heer, Science **297**, 787 (2002).

[13] S. B. Sinnott and R. Andrews, Crit. Rev. Solid State Mater. Sci. **26**, 145 (2001).

[14] S. Y. Hong *et al.*, J. Am. Chem. Soc. **129**, 10966 (2007).

[15] Z. Mao and S. B. Sinnott, J. Phys. Chem. B **105**, 6916 (2001).

[16] V. V. Simonyan, P. Diep, and J. K. Johnson, J. Chem. Phys. **111**, 9778 (1999).

[17] D. Cao, X. Zhang, J. Chen, W. Wang, and J. Yun, J. Phys. Chem. B **107**, 13286 (2003).

[18] P. Kowalczyk, L. Solarz, D. D. Do, A. Samborski, and J. M. D. MacElroy, Langmuir **22**, 9035 (2006).

[19] S. Agnihotri, Y. Zheng, J. P. B. Mota, I. Ivanov, and P. C. Kim, J. Phys. Chem. C **111**, 13747 (2007).

[20] G. Stan, M. J. Bojan, S. Curtarolo, S. M. Gatica, and M. W. Cole, Phys. Rev. B **62**, 2173 (2000).

[21] M. M. Calbi, S. M. Gatica, M. J. Bojan, and M. W. Cole, J. Chem. Phys. **115**, 9975 (2001).

[22] T. N. Antsygina, I. I. Poltavsky, and K. A. Chishko, Phys. Rev. B **74**, 205429 (2006).

[23] M. M. Calbi and M. W. Cole, Phys. Rev. B **66**, 115413 (2002).

[24] M. R. Johnson, S. Rolsa, P. Wassa, M. Murisc, and M. Bienfait, Chem. Phys. **293**, 217 (2003).

[25] M. R. LaBrosse, W. Shi, and J. K. Johnson, Langmuir **24**, 9430 (2008).

[26] S. E. Weber, S. Talapatra, C. Journet, A. Zambano, and A. D. Migone, Phys. Rev. B **61**, 13150 (2000).

[27] S. Talapatra and A. D. Migone, Phys. Rev. B **65**, 045416 (2002).

[28] W. Shi and J. K. Johnson, Phys. Rev. Lett. **91**, 015504 (2003).

[29] M. Bienfait, P. Zeppenfeld, N. Dupont-Pavlovsky, M. Muris, M. R. Johnson, T. Wilson, M. DePies, and O. E. Vilches, Phys. Rev. B **70**, 035410 (2004).

[30] D. S. Rawat, M. M. Calbi, and A. D. Migone, J. Phys. Chem. C **111**, 12980 (2007).

[31] D. S. Rawat, V. Krungleviciute, L. Heroux, M. Bulut, M. M. Calbi, and A. D. Migone, Langmuir **24**, 13465 (2008).

[32] J. Jiang, S. I. Sandler, M. Schenk, and B. Smit, Phys. Rev. B **72**, 045447 (2005).

[33] F. J. A. L. Cruz, I. A. A. C. Esteves, J. P. B. Mota, S. Agnihotri, E. A. Müller, and J. Nanosci, Nanotechnology (to be published).

[34] D. D. Do, H. D. Do, A. Wongkoblapa, and D. Nicholson, Phys. Chem. Chem. Phys. **10**, 7293 (2008).

[35] I. A. A. C. Esteves, F. J. A. L. Cruz, E. A. Muller, S. Agnihotri, and J. P. B. Mota, Carbon **47**, 948 (2009).

[36] S. Agnihotri, M. J. Rood, and M. Rostam-Abadi, Carbon **43**, 2379 (2005).

[37] S. Agnihotri, J. P. B. Mota, M. Rostam-Abadi, and M. J. Rood, J. Phys. Chem. B **110**, 7640 (2006).

[38] S. Agnihotri, P. Kim, Y. Zheng, J. P. B. Mota, and L. Yang, Langmuir **24**, 5746 (2008).

[39] A. N. Enyashin, S. Gemming, and G. Seifert, Nanotechnology **18**, 245702 (2007).

[40] M. C. Hersam, Nat. Nanotechnol. **3**, 387 (2008).

[41] R. M. Tromp, A. Afzali, M. Freitag, D. B. Mitzi, and Z. Chen, Nano Lett. **8**, 469 (2008).

[42] L. Zhang, S. Zaric, X. Tu, X. Wang, W. Zhao, and H. Dai, J. Am. Chem. Soc. **130**, 2686 (2008).

[43] D. Nicholson and N. G. Parsonage, *Computer Simulation and the Statistical Mechanics of Adsorption* (Academic Press, New York, 1982).

[44] M. P. Allen and D. J. Tildesley, *Computer Simulation of Liquids* (Clarendon Press, Oxford, 1990).

[45] D. Frenkel and B. Smit, *Understanding Molecular Simulation*, 2nd ed. (Academic Press, San Diego, 2002).

[46] M. G. Martin and J. I. Siepmann, J. Phys. Chem. B **102**, 2569 (1998).

[47] C. D. Wick, M. G. Martin, and J. I. Siepmann, J. Phys. Chem. B **104**, 8008 (2000).

[48] W. A. Steele, *The Interaction of Gases with Solid Surfaces* (Pergamon Press, Oxford, 1974).

[49] W. A. Steele, Surf. Sci. **36**, 317 (1973).

[50] W. A. Steele, Chem. Rev. **93**, 2355 (1993).

[51] J. S. Rowlinson and F. L. Swinton, *Liquids and Liquid Mixtures* (Butterworths, London, 1982).

[52] S. Agnihotri, J. P. B. Mota, M. Rostam-Abadi, and M. J. Rood, Langmuir **21**, 896 (2005).

[53] J. I. Siepmann, Mol. Phys. **70**, 1145 (1990).

[54] J. I. Siepmann and D. Frenkel, Mol. Phys. **75**, 59 (1992).

[55] D. Frenkel, G. C. A. Mooij, and B. Smit, J. Phys.: Condens. Matter **4**, 3053 (1992).

[56] J. de Pablo, M. Laso, and U. W. Sutter, J. Chem. Phys. **96**, 2395 (1992).

[57] R. C. Reid, J. M. Prausnitz, and B. E. Poling, *The Properties of Gases and Liquids* (McGraw-Hill, Singapore, 1988).

[58] The values of p_0 are (Ref. 57) 116.4 (CH_4), 37.6 (C_2H_4), 42.1 (C_2H_6), 11.5 (C_3H_6), and 9.53 bar (C_3H_8). For CH_4 and C_2H_4, which are supercritical fluids at the temperature explored here, the concept of saturation pressure does not exist and p_0 is replaced by a pseudovalue (Ref. 66) given by $p_c(T/T_c)^2$, where p_c and T_c are the critical pressure and temperature.

[59] K. Kaneko, R. F. Cracknell, and D. Nicholson, Langmuir **10**, 4606 (1994).

[60] F. J. A. L. Cruz and E. A. Müller, Adsorption **15**, 1 (2009).

[61] J. P. B. Mota and I. A. A. C. Esteves, Adsorption **13**, 21 (2007).

[62] D. S. Rawat and A. D. Migone, Phys. Rev. B **75**, 195440 (2007).

[63] The relation between q_{st} and the binding energy, E, for an adsorbed film (Ref. 62) is given by $q_{st}=E+\gamma k_B T$, where γ is a

constant that depends on the dimensionality of the adsorbed film; $\gamma=2$ for one-dimensional adsorption.

[64] V. Majer and V. Svoboda, *Enthalpies of Vaporization of Organic Compounds: A Critical Review and Data Compilation* (Blackwell Scientific Publications, Oxford, 1985).

[65] R. F. Cracknell and D. Nicholson, J. Chem. Soc., Faraday Trans. **90**, 1487 (1994).

[66] R. K. Agarwal and J. A. Schwarz, Carbon **26**, 873 (1988).